Geophys. J. Int. (2009) **176,** 405–414 doi: 10.1111/j.1365-246X.2008.04003.x

The point-spread function measure of resolution for the 3-D electrical resistivity experiment

Greg A. Oldenborger[1]* and Partha S. Routh[2]†

[1]*Department of Earth and Ocean Sciences, University of British Columbia,* 6339 *Stores Road, Vancouver,* BC V6T 1Z4*, Canada. E-mails: goldenbo@NRCan.gc.ca*

[2]*Department of Geosciences, Boise State University,* 1910 *University Drive, Boise,* ID 83725

Accepted 2008 October 7. Received 2008 September 4; in original form 2007 July 5

SUMMARY

The solution appraisal component of the inverse problem involves investigation of the relationship between our estimated model and the actual model. However, full appraisal is difficult for large 3-D problems such as electrical resistivity tomography (ERT). We tackle the appraisal problem for 3-D ERT via the point-spread functions (PSFs) of the linearized resolution matrix. The PSFs represent the impulse response of the inverse solution and quantify our parameter-specific resolving capability. We implement an iterative least-squares solution of the PSF for the ERT experiment, using on-the-fly calculation of the sensitivity via an adjoint integral equation with stored Green's functions and subgrid reduction. For a synthetic example, analysis of individual PSFs demonstrates the truly 3-D character of the resolution. The PSFs for the ERT experiment are Gaussian-like in shape, with directional asymmetry and significant off-diagonal features. Computation of attributes representative of the blurring and localization of the PSF reveal significant spatial dependence of the resolution with some correlation to the electrode infrastructure. Application to a time-lapse ground-water monitoring experiment demonstrates the utility of the PSF for assessing feature discrimination, predicting artefacts and identifying model dependence of resolution. For a judicious selection of model parameters, we analyse the PSFs and their attributes to quantify the case-specific localized resolving capability and its variability over regions of interest. We observe approximate interborehole resolving capability of less than 1–1.5 m in the vertical direction and less than 1–2.5 m in the horizontal direction. Resolving capability deteriorates significantly outside the electrode infrastructure.

Key words: Inverse theory; Tomography; Electrical properties; Hydrogeophysics; Hydrology.

1 INTRODUCTION

The crux of any inverse problem is often considered to be the estimation component, whereby we construct a model estimate to fit our data. However, the credibility of geophysical inversion or tomography suffers from a lack of quantification of the reliability of our model estimates. Although we often cannot establish the true accuracy of our model estimate, the tools of solution appraisal allow for an investigation of the relationship between our estimated model and the actual model.

For small linear problems, solution appraisal is relatively straightforward (e.g. Menke 1989). This is not so for non-linear problems, since no formal theory exists to deal with solution appraisal (Oldenburg 1983; Snieder 1998). In addition, for large 3-D problems with multiscale model domains, the computational burden of solution appraisal can be prohibitive (Nolet *et al.* 1999). The 3-D electrical resistivity tomography (ERT) problem is both non-linear and large with several thousands of data and several hundreds of thousands of model parameters.

Furthermore, the full appraisal problem has both an error propagation aspect and a resolution aspect. Since data noise is an implicit component of the resolving capability, we focus only on the model resolution (Backus & Gilbert 1968; Menke 1989). Since the ERT problem is non-linear, we employ the linearized form of the resolution. Ultimately, it is unlikely that geophysical inversion will ever exist in absence of an interpreter or decision maker, (Scales & Snieder 2000) and when faced with geophysical

*Now at: Geological Survey of Canada, Natural Resources Canada, 601 Booth Street, Ottawa, ON K1A 0E8, Canada

†Now at: Seismic Technology Development, ConocoPhillips, 600 North Dairy Ashford Street, Houston, TX 77079.

images, some pragmatic measure of reliability can only benefit the interpreter.

The discrete linearized resolution matrix has been applied to the 2-D resistivity experiment, primarily in a diagonalized sense (Ramirez *et al.* 1993, 1995), but also in terms of attributes of the full resolution matrix (Friedel 2003). However, for 3-D problems, computing the full model resolution matrix remains difficult and expensive. Alternatively, Alumbaugh & Newman (2000) compute a decimated model resolution matrix for the 3-D electromagnetic experiment, using a column-wise iterative solution. Following this approach, we implement a column-wise iterative solution of the model resolution matrix for the 3-D ERT experiment. Rather than computing a decimated resolution matrix, we focus on the individual columns of interest, each of which represents a point-spread function (PSF) that quantifies the parameter-specific (localized) model resolution (Parker 1994).

We first develop a technique for computing individual PSFs for the 3-D ERT experiment. For a synthetic example, analysis of a judicious selection of PSFs demonstrates the truly 3-D character of our resolving capability in a linearized sense. The spatial variability of resolution over the model domain can be quantified via PSF attributes that are indicative of blurring and localization. Application of the PSF to a time-lapse ground-water remediation experiment demonstrates the utility of the PSF and its attributes for judging our abilities of feature discrimination, for predicting artefacts and for identifying model dependence of resolution. Used in such a fashion, the PSF can provide a powerful tool for solution appraisal of 3-D ERT.

2 MODEL RESOLUTION

The PSF can be viewed as a component of the model resolution, which can be exactly defined for linear inverse problems (Backus & Gilbert 1968). In general, resolution of the linearized problem is applied and accepted as the resolution for models that are 'close' to the actual solution (Menke 1989). Consider the discrete non-linear problem described as $f(\mathbf{m}) = \mathbf{d}$ where $\mathbf{m}$ is the model vector, $\mathbf{d}$ is the data vector and f is the forward operator describing the physics. For an overparametrized or underdetermined problem, we construct the regularized least-squares objective function

$$\psi = \{\mathbf{W}_\mathrm{d}[\mathbf{d} - f(\mathbf{m})]\}^\mathrm{T}\{\mathbf{W}_\mathrm{d}[\mathbf{d} - f(\mathbf{m})]\} + \mu\left[\mathbf{W}_\mathrm{m}(\mathbf{m} - \mathbf{m}^\mathrm{ref})\right]^\mathrm{T}\left[\mathbf{W}_\mathrm{m}(\mathbf{m} - \mathbf{m}^\mathrm{ref})\right], \quad (1)$$

which has both data and model components related by the trade-off parameter μ. The data are weighted by the matrix $\mathbf{W}_\mathrm{d}$ and the model is weighted by $\mathbf{W}_\mathrm{m}$ with respect to some reference $\mathbf{m}^\mathrm{ref}$.

Linearization involves a Taylor expansion of the forward operator about the ith model estimate. Neglecting terms of $\mathcal{O}(||\Delta\mathbf{m}||^2)$, the expression for the updated model is

$$\mathbf{m}^{i+1} = \mathbf{H}^{-1}\left\{\mathbf{S}^\mathrm{T}\mathbf{W}_\mathrm{d}^\mathrm{T}\mathbf{W}_\mathrm{d}[\mathbf{d} - f(\mathbf{m}^i) + \mathbf{S}\mathbf{m}^i - \mathbf{S}\mathbf{m}^\mathrm{ref}]\right\} + \mathbf{m}^\mathrm{ref}, \quad (2)$$

where $S_{j\mathrm{k}} = \partial f_j/\partial m_k$ is the sensitivity of the jth datum to the kth model parameter evaluated at the ith model and

$$\mathbf{H} = \left[\mathbf{S}^\mathrm{T}\mathbf{W}_\mathrm{d}^\mathrm{T}\mathbf{W}_\mathrm{d}\mathbf{S} + \mu\mathbf{W}_\mathrm{d}^\mathrm{T}\mathbf{W}_\mathrm{d}\right]. \quad (3)$$

To quantify the relationship between the estimated model and the actual model, we realize that the observed data are a function of the actual model $\tilde{\mathbf{m}}$ according to

$$\mathbf{d} = f(\tilde{\mathbf{m}}) + \mathbf{e}^\mathrm{s} + \mathbf{e}^\mathrm{r}, \quad (4)$$

where $\mathbf{e}^\mathrm{r}$ is the random measurement error and $\mathbf{e}^\mathrm{s}$ is the systematic error due to discretization, incorrect model physics (van Wijk *et al.* 2002) or experimental errors (Oldenborger *et al.* 2005). In the non-linear case, Backus & Gilbert (1970) and Alumbaugh & Newman (2000) posit that, at the end of the iterative procedure, the model estimate is linearly close to the actual model $\tilde{\mathbf{m}}$ such that we can write $\tilde{\mathbf{m}} = \mathbf{m}^i + \Delta\tilde{\mathbf{m}}$, where $\Delta\tilde{\mathbf{m}}$ would be the update required to achieve the actual model. Via first-order Taylor expansion of $f(\tilde{\mathbf{m}})$, we have $\mathbf{d} - f(\mathbf{m}^i) = \mathbf{S}\Delta\tilde{\mathbf{m}} + \mathbf{e} = \mathbf{S}\tilde{\mathbf{m}} - \mathbf{S}\mathbf{m}^i + \mathbf{e}$, where we have lumped the error terms including any linearization error. Substitution into the model estimate (eq. 2) yields

$$\mathbf{m}^{i+1} = \mathbf{H}^{-1}\mathbf{S}^\mathrm{T}\mathbf{W}_\mathrm{d}^\mathrm{T}\mathbf{W}_\mathrm{d}\mathbf{S}\,\tilde{\mathbf{m}} + \mathbf{H}^{-1}\mathbf{S}^\mathrm{T}\mathbf{W}_\mathrm{d}^\mathrm{T}\mathbf{W}_\mathrm{d}\,\mathbf{e} - \mathbf{H}^{-1}\mathbf{S}^\mathrm{T}\mathbf{W}_\mathrm{d}^\mathrm{T}\mathbf{W}_\mathrm{d}\mathbf{S}\,\mathbf{m}^\mathrm{ref} + \mathbf{m}^\mathrm{ref}, \quad (5)$$

which we can write more compactly as

$$\mathbf{m}_\mathrm{b} = \mathbf{m}^{i+1} - [\mathbf{I} - \mathbf{R}]\mathbf{m}^\mathrm{ref} = \mathbf{R}\tilde{\mathbf{m}} + \mathbf{n}, \quad (6)$$

where $\mathbf{m}_\mathrm{b}$ is the unbiased model estimate, $\mathbf{n}$ is the noise term, $[\mathbf{I} - \mathbf{R}]$ is the blurring matrix and $\mathbf{R}$ is the linearized resolution matrix defined as

$$\mathbf{R} = \left[\mathbf{S}^\mathrm{T}\mathbf{W}_\mathrm{d}^\mathrm{T}\mathbf{W}_\mathrm{d}\mathbf{S} + \mu\mathbf{W}_\mathrm{m}^\mathrm{T}\mathbf{W}_\mathrm{m}\right]^{-1}\mathbf{S}^\mathrm{T}\mathbf{W}_\mathrm{d}^\mathrm{T}\mathbf{W}_\mathrm{d}\mathbf{S}. \quad (7)$$

In general, we assume that $\mathbf{n}$ is zero-mean and relatively small. Furthermore, Oldenborger *et al.* (2007b) demonstrate that the blurring term for the ERT experiment is near zero over the volume of investigation, such that $\mathbf{m} \approx \mathbf{R}\tilde{\mathbf{m}}$. As such, the linearized resolution matrix provides a measure of resolving power for models that are linearly close to the actual model. Ideally, the resolution matrix equals the identity matrix and the estimated model is exactly resolved. However, for under- or mixed-determined problems, $\mathbf{R}$ departs from the identity and is generally asymmetric for any non-diagonal regularization.

3 POINT-SPREAD FUNCTIONS

Consider dividing $\mathbf{R}$ into its column vectors $\mathbf{p}_k$ and row vectors $\mathbf{a}_\ell$ for an M-parameter model domain:

$$\mathbf{R} = \begin{bmatrix} \mathbf{a}_1 \\ \vdots \\ \mathbf{a}_\ell \\ \vdots \\ \mathbf{a}_M \end{bmatrix} = \begin{bmatrix} \mathbf{p}_1 & \cdots & \mathbf{p}_k & \cdots & \mathbf{p}_M \end{bmatrix}. \quad (8)$$

Since $\mathbf{m} \approx \mathbf{R}\tilde{\mathbf{m}}$, the rules of matrix algebra dictate that $m_\ell \approx \mathbf{a}_\ell\,\tilde{\mathbf{m}}$ such that the ℓth row of $\mathbf{R}$ determines what linear combination of the actual model parameters forms the ℓth estimated parameter. The row $\mathbf{a}_\ell$ describes the mapping of the actual model to the ℓth estimated parameter and is the equivalent to the averaging function (AF) of Backus & Gilbert (1968).

Conversely, we have

$$\mathbf{m} \approx \sum_{k=1}^{M} \tilde{m}_k\mathbf{p}_k, \quad (9)$$

so that the estimated model is a linear combination of columns $\mathbf{p}_k$. The kth column of $\mathbf{R}$ determines how the kth actual parameter is mapped to the estimated model. In other words, $\mathbf{p}_k$ represents how a delta function perturbation in the kth actual parameter propagates

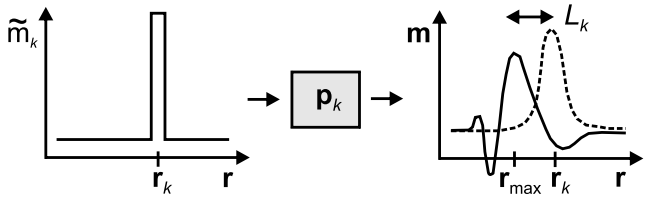

Figure 1. Each PSF represents the estimated model (right-hand panel) for a delta function perturbation in the corresponding actual model parameter (left-hand panel). For the kth parameter, the most desirable PSF is a delta-like function centred on $\mathbf{r}_k$ (dashed). In practice (solid), we may observe blurring, side lobes and localization error L_k, all off-diagonal effects.

to our estimated model, as illustrated in Fig. 1. For this reason, the columns of the resolution matrix are termed the PSFs.

The set of all PSFs 'or' AFs comprises the full model resolution matrix and both the PSF and AF are ideally delta-like functions located at the parameter of interest (on the diagonal). It is perhaps for these reasons that there is some conflation of terminology in the geophysical literature regarding AFs versus PSFs. Friedel (2003) computes the AFs, refers to them as PSFs and discusses the results in the context of both parameter averaging and parameter resolution. Alumbaugh & Newman (2000) compute the PSF but refer to it as the AF and interpret results in terms of parameter averaging. However, there is a distinct difference between the PSF and AF as described above. It makes no sense to accept a well-defined average of a poorly-resolved model parameter. Miller & Routh (2007) demonstrate such a situation characterized by a delta-like AF and a flat PSF. That said, some non-regularized inverse formulations result in equivalency of the AF and PSF (e.g. Parker 1994, p. 211), and generalized inversion methods, such as singular value decomposition, may result in a symmetric resolution matrix. Regardless, given the general asymmetry of $\mathbf{R}$, it is the PSF that provides the parameter-specific resolving capability.

3.1 PSF attributes

When describing resolving capability of individual PSFs, we will utilize the concepts of 'blurring' and 'localization'. Blurring refers to the spread of the PSF and is thus a measure of how the inversion routine disperses information. To quantify blurring, we propose the directional 'spread' attribute defined in the x-direction for example as

$$s_x(\mathbf{r}_k) = \left[\frac{\int (x - x_k)^2 p_k^2(\mathbf{r}) \mathrm{d}^3\mathbf{r}}{\alpha + \int p_k^2(\mathbf{r}) \mathrm{d}^3\mathbf{r}}\right]^{1/2}, \tag{10}$$

where $\mathbf{r}_k$ is the position vector of the kth model parameter and α is some small constant to account for the possibility of zero-energy PSF. The spread attribute is similar to a second spatial moment, but involves the squared PSF to enforce positivity.

Although the spread does account for off-centre energy in the PSF, it is important to isolate the degree of localization error, whereby the PSFs attains a maximum value at $\mathbf{r}_{\max} \neq \mathbf{r}_k$. Non-zero localization error occurs for off-diagonal maxima of $\mathbf{R}$ and implies an inability of the inversion routine to accurately position the impulse response. In 2-D, Friedel (2003) implements a 'distortion flag' to indicate off-diagonal maxima of $\mathbf{R}$. We adopt the 3-D measure of the localization error L proposed by Pascual-Marqui (1999),

$$L(\mathbf{r}_k) = ||\mathbf{r}_k - \mathbf{r}_{\max}||, \tag{11}$$

who argues that, regardless of blurring, we cannot have good resolution without good localization. Conversely, correct localization does not necessarily imply good resolution. The localization error is easily cast in a 3-component directional form.

Finally, the departure of the PSF from a delta function (hereafter, the 'departure') combines the effects of spread and localization error (Routh *et al.* 2005). The 3-D departure is expressed as

$$d(\mathbf{r}_k) = \left[\frac{\int w(\mathbf{r})[p_k(\mathbf{r}) - \Delta_k(\mathbf{r})]^2 \mathrm{d}^3\mathbf{r}}{\alpha + \int p_k^2(\mathbf{r}) \mathrm{d}^3\mathbf{r}}\right]^{1/2}. \tag{12}$$

where $\Delta_k(\mathbf{r}) = 1$, for $\mathbf{r} = \mathbf{r}_k$, and 0, otherwise. The weighting term $w(\mathbf{r}) = 1 + |\mathbf{r} - \mathbf{r}_k|/\lambda$ penalizes off-diagonal features based on some length scale that we set as $\lambda = 1$ m.

3.2 PSF computation for 3-D ERT

For large 3-D problems, calculation of the resolution matrix is difficult because the generalized inverse cannot be formed (Nolet *et al.* 1999). The inverse problem is solved via iterative methods and, in most cases, this circumvents the need to invert products of the form $\mathbf{S}^{\mathrm{T}}\,\mathbf{S}$. For such problems, Alumbaugh & Newman (2000) demonstrate how we can also use iterative methods to calculate individual PSFs or the full $\mathbf{R}$. We start with the definition of the linearized resolution

$$\mathbf{R} = [\mathbf{J}^{\mathrm{T}}\mathbf{J} + \mu\mathbf{W}_{\mathrm{m}}^{\mathrm{T}}\mathbf{W}_{\mathrm{m}}]^{-1}\mathbf{J}^{\mathrm{T}}\mathbf{J}, \tag{13}$$

where we have normalized the sensitivity by the data weighting $\mathbf{J} = \mathbf{W}_{\mathrm{d}}\mathbf{S}$.

As per Alumbaugh & Newman (2000), we isolate the kth column by using the delta-function vector Δ_k that is equal to unity at the kth element and zero elsewhere, so that $\mathbf{p}_k = \mathbf{R}\Delta_k$ and

$$[\mathbf{J}^{\mathrm{T}}\mathbf{J} + \mu\mathbf{W}_{\mathrm{m}}^{\mathrm{T}}\mathbf{W}_{\mathrm{m}}]\mathbf{p}_k = \mathbf{J}^{\mathrm{T}}\mathbf{J}\Delta_k. \tag{14}$$

It is from eq. (14) that we see the model construction nature of the PSF in that $\mathbf{p}_k$ is our best regularized least-squares estimate of the delta function. Although the effect of noise is not explicit to eq. (14), it is implicit via the weighting of $\mathbf{J}$ and the choice of μ.

To avoid explicit inversion of the left-hand side of eq. (14), we recover the PSF via iterative least-squares solution of the system

$$\begin{bmatrix} \mathbf{J} \\ \sqrt{\mu}\,\mathbf{W}_{\mathrm{m}} \end{bmatrix} \mathbf{p}_k = \begin{bmatrix} \mathbf{J}\Delta_k \\ 0 \end{bmatrix}, \tag{15}$$

using conjugate gradients applied to the normal equations (CGLS, e.g. Press *et al.* 1992; Golub & Van Loan 1996; Routh *et al.* 2005). Within the CGLS algorithm, we require matrix vector products of the form $\mathbf{J}\mathbf{v}$, $\mathbf{J}^{\mathrm{T}}\mathbf{v}$, $\mathbf{W}_{\mathrm{m}}\mathbf{v}$ and $\mathbf{W}_{\mathrm{m}}^{\mathrm{T}}\mathbf{v}$. The model weighting matrix is sparse so that storage and matrix–vector multiplication of $\mathbf{W}_{\mathrm{m}}$ are inexpensive. The sensitivity matrix, however, is full. To avoid storage costs, Li & Oldenburg (2000) build and compress $\mathbf{J}$ using a wavelet transform. Alternatively, to form $\mathbf{J}\mathbf{v}$ element-wise requires only a single row of $\mathbf{J}$ at a time and to form $\mathbf{J}^{\mathrm{T}}\mathbf{v}$ element-wise requires only a single column of $\mathbf{J}$ at a time. Zhang *et al.* (1995) utilize this element-wise operation to show that the products $\mathbf{J}\mathbf{v}$ and $\mathbf{J}^{\mathrm{T}}\mathbf{v}$ can be formed, each by the solution of a single forward problem. However, solving the matrix–vector products via forward modelling is expensive for any appreciable number of CGLS iterations and is only applicable for constant boundary conditions, not for source-dependent boundary conditions (Zhou & Greenhalgh 2001; Oldenborger & Routh 2006).

To avoid compression of $\mathbf{J}$ or forward modelling within the CGLS algorithm, we form the products $\mathbf{J}\mathbf{v}$ and $\mathbf{J}^{\mathrm{T}}\mathbf{v}$ element-wise, using on-the-fly calculation of $\mathbf{J}$. By storing the pole–pole Green's functions for every electrode in an ERT experiment, we are able to build any

element of **J** using an adjoint integral equation similar to that of Park & Van (1991). The sensitivity with respect to $m_k = \ln(\sigma_k)$ is

$$J_{jk} = -\frac{1}{\eta_j} \int_{V_k} \sigma_k \nabla \mathcal{G}_j^{\mathrm{A}} \cdot \nabla \mathcal{G}_j \, \mathrm{d}V_k, \tag{16}$$

where $\mathcal{G}_j$ and $\mathcal{G}_j^{\mathrm{R}}$ are the superposed pole–pole Green's functions and adjoint (reciprocal) Green's functions associated with the jth quadrupole datum with noise estimate η_j. The integral is evaluated piecewise over the volume of the kth model parameter with conductivity σ_k.

3.3 Subgrid reduction

At any given time, in addition to the Green's functions, we need only to hold in memory either a single row or a single column of the sensitivity matrix. According to eq. (16), on-the-fly calculation of a column of the sensitivity matrix involves cycling over all data for a particular model parameter. Similarly, on-the-fly calculation of a row of the sensitivity matrix involves evaluating eq. (16) while cycling over the entire model domain for a particular datum. Forming $\mathbf{J}^{\mathrm{T}}\mathbf{v}$ requires calculation of M rows and forming $\mathbf{J}\mathbf{v}$ requires calculation of N columns, all for a single PSF for a single model parameter.

Therefore, although on-the-fly calculation of **J** is memory efficient, it can be slow for large models. To increase computational speed, the potential exists to farm out the element-wise calculation of $\mathbf{J}\mathbf{v}$ and $\mathbf{J}^{\mathrm{T}}\mathbf{v}$ to a system of parallel processors. Alternatively, we implement a form of domain reduction that reduces the number of active model parameters.

The Green's functions for any given model are computed on an expansive numerical grid, using a weak-form finite-volume technique (Dey & Morrison 1979; Oldenborger & Routh 2006). The expansive grid is necessary to accommodate the boundary conditions assigned to the Green's functions.

However, the adjoint integral calculation of **J** according to eq. (16) does not require definition of boundary conditions of any sort. As such, **J** and $\mathbf{p}_k$ can be computed on a numerical grid of reduced extent. The reduced grid, or subgrid, is simply a subset of the expansive grid with its associated Green's functions; there is no upscaling. The accurately computed Green's functions from the interior of the expansive grid are transferred to the boundary and interior points of the reduced subgrid. This domain reduction introduces no error to the calculation of **J** that is not inherent to the calculation of the Green's functions.

Even with domain reduction, the amount of information involved in the analysis of the full set of PSFs over the entire model domain is large—a 3-D function (the PSF) for every parameter in the reduced model domain. For characterization of the 3-D nature of the resolving capability, visual analysis of the PSF is necessary, but impractical for the full set of PSFs. Alternatively, we will judiciously select a small set of PSFs at positions that we expect to be informative of the resolution of a particular experiment. These individual PSFs give us an indication of the blurring, the localization, the directional asymmetry and the occurrence of side-lobes. For larger sets of PSFs, we will utilize the attributes of spread, localization error and departure to quantify the spatial variability of the resolving capability.

4 SYNTHETIC ERT EXAMPLE

Our synthetic example is constructed to mimic a 3-D ERT installation in a shallow unconfined alluvial aquifer with a pre-existing

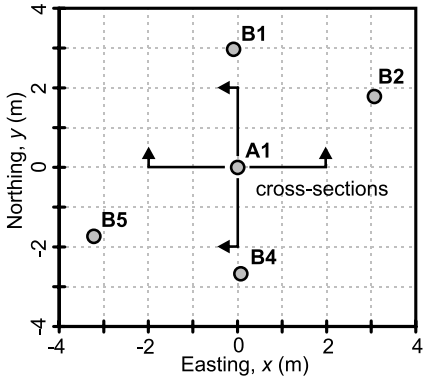

Figure 2. Schematic representation of borehole infrastructure. The lines of cross-section indicate views to be illustrated in subsequent figures that are both in-plane and out-of-plane with respect to the boreholes. The northing cross-section intersects boreholes B4, A1 and B1, whereas the easting cross-section intersects only A1.

borehole infrastructure illustrated in Fig. 2. Borehole A1 and the surrounding boreholes B1, B2, B4 and B5 are each instrumented with 28 electrodes, spaced at 0.5 m intervals from 2.1–15.6 m depth below land surface at A1. The aquifer model consists of an unsaturated zone to 2 m depth ($\sigma = 0.2\,\mathrm{mS\,m^{-1}}$) over a saturated zone ($\sigma = 1.5\,\mathrm{mS\,m^{-1}}$). To simulate a conductive contaminant, we add a conductive zone ($\sigma = 30\,\mathrm{mS\,m^{-1}}$) extending to ± 0.75 m in the horizontal directions and from 5– 13 m depth surrounded by a less-conductive zone ($\sigma = 10\,\mathrm{mS\,m^{-1}}$) extending to ± 1.5 m in the horizontal directions and from 3– 15 m depth (Fig. 3a). The model is parametrized using a finite-volume mesh comprised of 282 567 conductivity cells ($58 \times 58 \times 84$) with 0.25 m cell sizes over the central borehole region. Outside of the borehole region, from ± 4 m outward and 18 m downward, the mesh expands by a factor of $\sqrt{2}$ to ± 80 m in the horizontal directions and 125 m in depth.

Synthetic ERT data are computed using a circulating skip-3 vertical dipole–dipole survey geometry (Oldenborger *et al.* 2007a). The complete data set includes full reciprocals and is comprised of 19 180 quadrupole measurements of potential difference per unit current. Each datum is contaminated with a random value drawn from a zero-mean normal distribution with a standard deviation equal to 4 per cent of the datum. The data are inverted using the 3-D regularized least-squares Gauss–Newton inversion of Li & Oldenburg (2000). The regularization parameter is determined from a line search and iteration proceeds until the misfit is equal to the level of noise assigned to the data. Fig. 3(b) illustrates the estimated model obtained from the synthetic data.

4.1 Synthetic PSFs

The 3-D PSF for a near-borehole target parameter in the northing section at 8 m depth is illustrated in Fig. 4(a). The character of the PSF is Gaussian-like in shape, but appears flattened in the horizontal directions. The degree of oscillation, or side-lobes, are minimal, although the PSF is observed to spike negative at borehole B1 away from the parameter of interest. The directional spreads for this PSF at 1 m from the borehole are $s_x = 1.6$ m, $s_y = 1.7$ m, $s_z = 1.3$ m, confirming directional dependence of our resolving capability with maximum resolution in the vertical direction. The localization error of 0.35 m associated with this model parameter is confined entirely to the horizontal plane and represents a diagonal offset of one cell to the northwest.

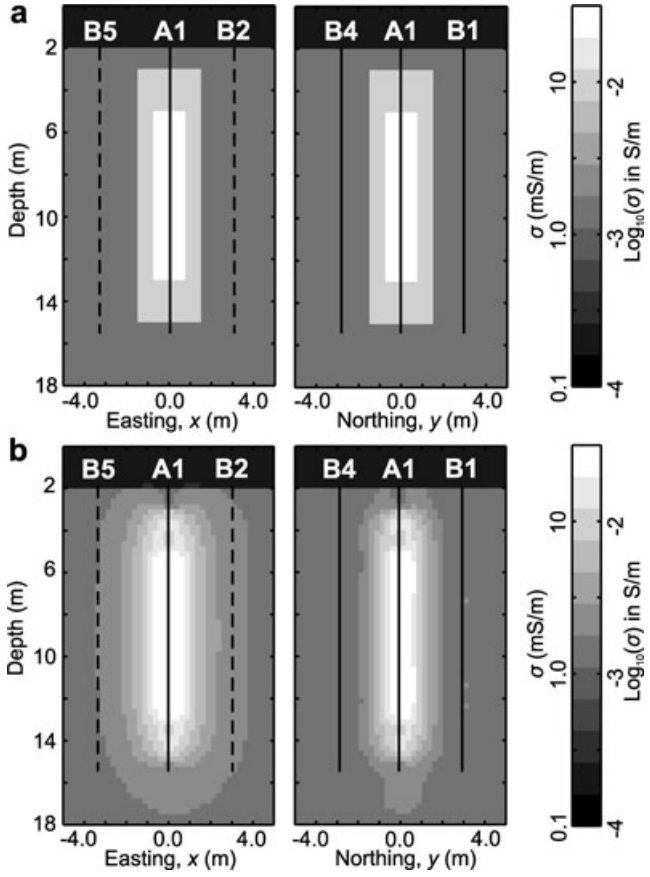

Figure 3. Cross-sections of (a) synthetic and (b) recovered electrical conductivity models. Dashed vertical lines indicate out-of-plane boreholes; solid vertical lines indicate in-plane boreholes.

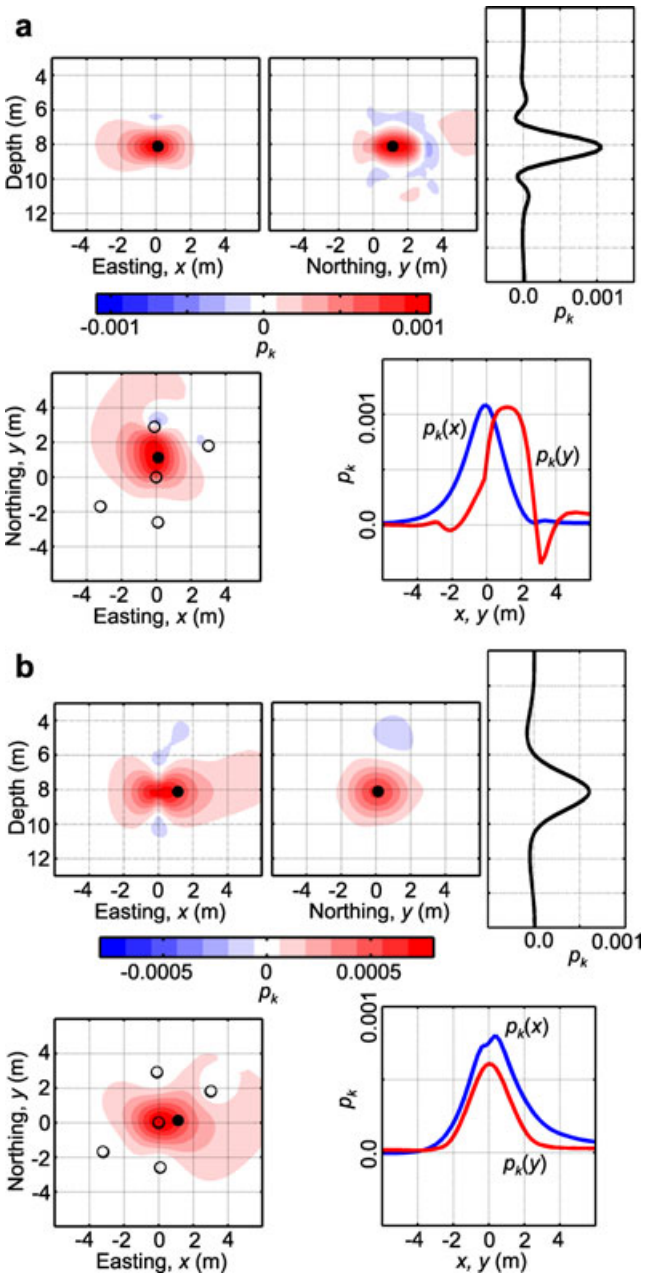

Figure 4. Synthetic PSFs at positions indicated by the black dots: (a) $\mathbf{r}_k = [0.125, 1.125, 8.125]$, (b) $\mathbf{r}_k = [1.125, 0.125, 8.125]$. The 2-D sections and 1-D profiles are taken through $\mathbf{r}_k$. Borehole locations are indicated by open circles.

For comparison, we consider the PSF for another near-borehole target parameter at the same depth but in the easting section, illustrated in Fig. 4(b). For this parameter at 1 m from the borehole, we observe increased blurring as demonstrated by the spreads $s_x = 2.1$ m, $s_y = 1.8$ m, $s_z = 1.7$ m. Furthermore, the centre of the PSF tends to be pulled towards the central borehole away from the parameter of interest (Fig. 4b, blue curve). The localization error of 0.75 m is entirely in x, and there is an asymmetric eastward spreading of the PSF. In contrast, the PSF at the borehole (not shown) exhibits much less blurring and the directional spreads are reduced to $s_x = 1.1$ m, $s_y = 1.2$ m, $s_z = 1.0$ m, with a localization error of 0.25 m in x.

The observations hold generally that the spread s, localization error L and departure d, all increase away from the boreholes and for parameters that are out-of-plane with respect to the borehole infrastructure (i.e. the easting section). This behaviour is summarized in Fig. 5 for the northing and easting directions. In the northing direction (Figs 5a and b), s, L and d all behave in a similar manner. The attributes are low at the central borehole A1, increase slightly in the interborehole region, decrease at the outer borehole B1 and then increase rapidly outside the borehole infrastructure. Beyond 5 m, the horizontal spreads s_x and s_y exceed 2 m (Fig. 5a) and L exceeds 1 m (Fig. 5b). In the easting direction (Figs 5c and d), there is only borehole A1 and the attribute behaviour is more complicated. Values of s_x and s_z oscillate (Fig 5c), whereas L and d increase away from A1 (Fig. 5d). Localization error is primarily constrained to the horizontal plane such that $x_{\max}$ and $y_{\max}$ are pulled towards the borehole infrastructure (Fig. 4b). In all cases, the attributes along the easting profile (Figs 5c and d) exceed those along the northing profile (Figs 5a and b). This reduced resolution in the easting direction is manifest as increased smoothing of the target boundary in the recovered conductivity model (Fig. 3b).

4.2 3-D PSF attributes

To examine PSF attributes in 3-D, we consider the small-scale model shown in Fig. 6, consisting of a conductive target ($\sigma = 30$ mS m^{-1}) in a resistive background ($\sigma = 1.5$ mS m^{-1}). The model is comprised of 2584 conductivity cells ($13 \times 13 \times 14$) with 1 m^3 cell sizes in the central region and an extent of ± 15 m in the horizontal directions

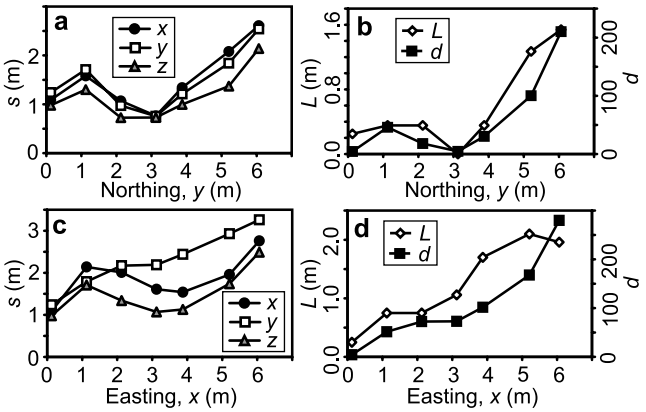

Figure 5. Synthetic PSF attributes at 8.125 m depth. (a) Directional spreads in the northing direction. (b) Localization error and departure from a delta function in the northing direction. (c) Directional spreads in the easting direction. (d) Localization error and departure from a delta function in the easting direction.

and 17 m in depth. The experiment consists of 544 non-reciprocal vertical dipole–dipole data taken over 40 electrodes: 8 per hole, from 2–9 m depth, at 1 m intervals. Inversion and PSF computations are performed as in the previous synthetic example, but in this case, we compute the full set of PSFs.

Given the full set of PSFs, we can build 3-D attribute volumes as illustrated in Fig. 7 (i.e. the PSF attributes for all model parameters). This process is different from and less expensive than building a 3-D attribute volume from a decimated resolution matrix (i.e. sparse PSFs) for the full-size synthetic problem. The 3-D attributes clearly demonstrate the increase in resolution from the *x*- to *y*- to *z*-direction over the entire model domain (Figs 7a–c). We also see that the localization error is low (below one cell size) within and just outside of the interborehole region. Outside of the core region, both *L* and *d* increase rapidly. The 3-D results illustrate that the different attributes are largely consistent and can be used to define some reliable region for the experiment.

5 EXPERIMENTAL ERT APPLICATION

We are interested in applying the PSF to inversion results obtained for ERT data collected during a tracer experiment (Oldenborger *et al.* 2007a). The experiment was designed to test the performance of ERT monitoring of a remediation effort for an unconfined aquifer. As a proxy contaminant, a conductive tracer consisting of 3740 L of 8420 ppm potassium bromide (KBr) solution was injected into the central borehole A1 (Fig. 2). ERT data were collected at pre-injection, post-injection and post-withdrawal stages of the experiment.

The survey geometry is the same as that described in the synthetic example. The numerical mesh is modified slightly and shifted downwards by 0.1 m to account for the measured water table depth of 1.9 m. The experimental data were inverted using the same algorithm as in the synthetic example with the 2-layer aquifer reference model. The experimental data noise is assumed to have a normally distributed component with a standard deviation equal to 2 per cent of each datum, plus the observed reciprocal error (approximately equal to 2 per cent of each datum), plus a constant floor of $0.08\ \mathrm{V\,A^{-1}}$.

Fig. 8 illustrates cross-sections of the recovered 3-D electrical conductivity model for the pre-injection experimental stage. Geoelectrical interpretation of the background electrical conductivity suggests zones of high electrical conductivity at 2–3 m depth, near 5.5 m depth, and at 11–13 m depth. These features are interpreted as potential preferential flow paths that show up as high porosity signals in thermal neutron logs (Barrash & Clemo 2002).

5.1 Pre-injection PSFs

The experimental PSFs for the northing and easting near-borehole parameters considered in the synthetic case are illustrated in Fig. 9. Again, the PSFs exhibit a flattened Gaussian-like shapes with some side lobes and asymmetry. Side lobes are more prevalent in the horizontal direction for the northing PSF (Fig. 9a) and in the vertical direction for the easting PSF (Fig. 9b). The vertical to horizontal resolving capability is approximately 2 : 1.

The experimental attributes in the northing and easting directions are illustrated in Fig. 10 at 8 m depth. Much like the synthetic

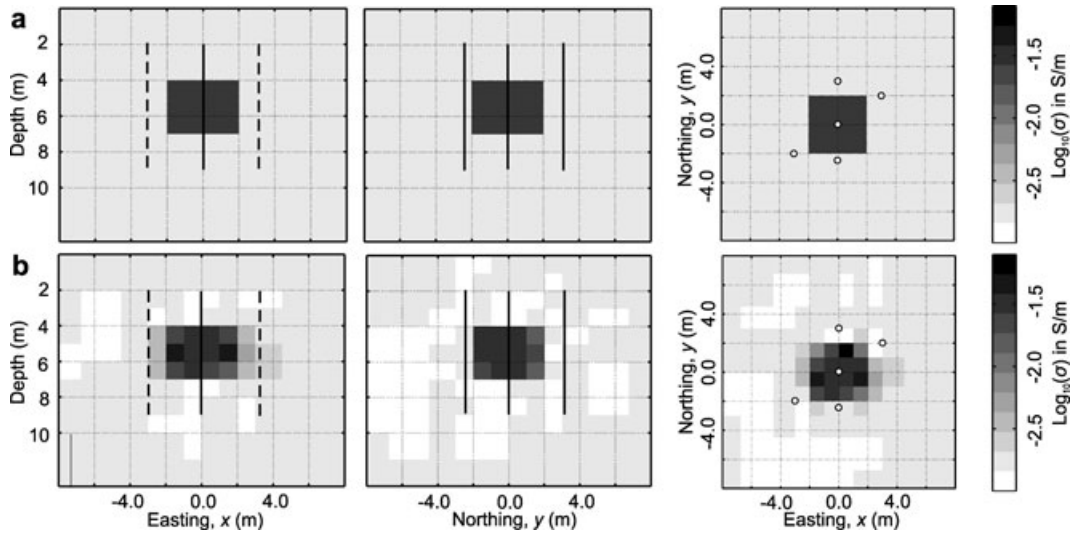

Figure 6. Cross-sections of small-scale (a) synthetic and (b) recovered electrical conductivity models. Dashed vertical lines indicate out-of-plane boreholes; solid vertical lines indicate in-plane boreholes. Horizontal slices are taken at 5.5 m depth.

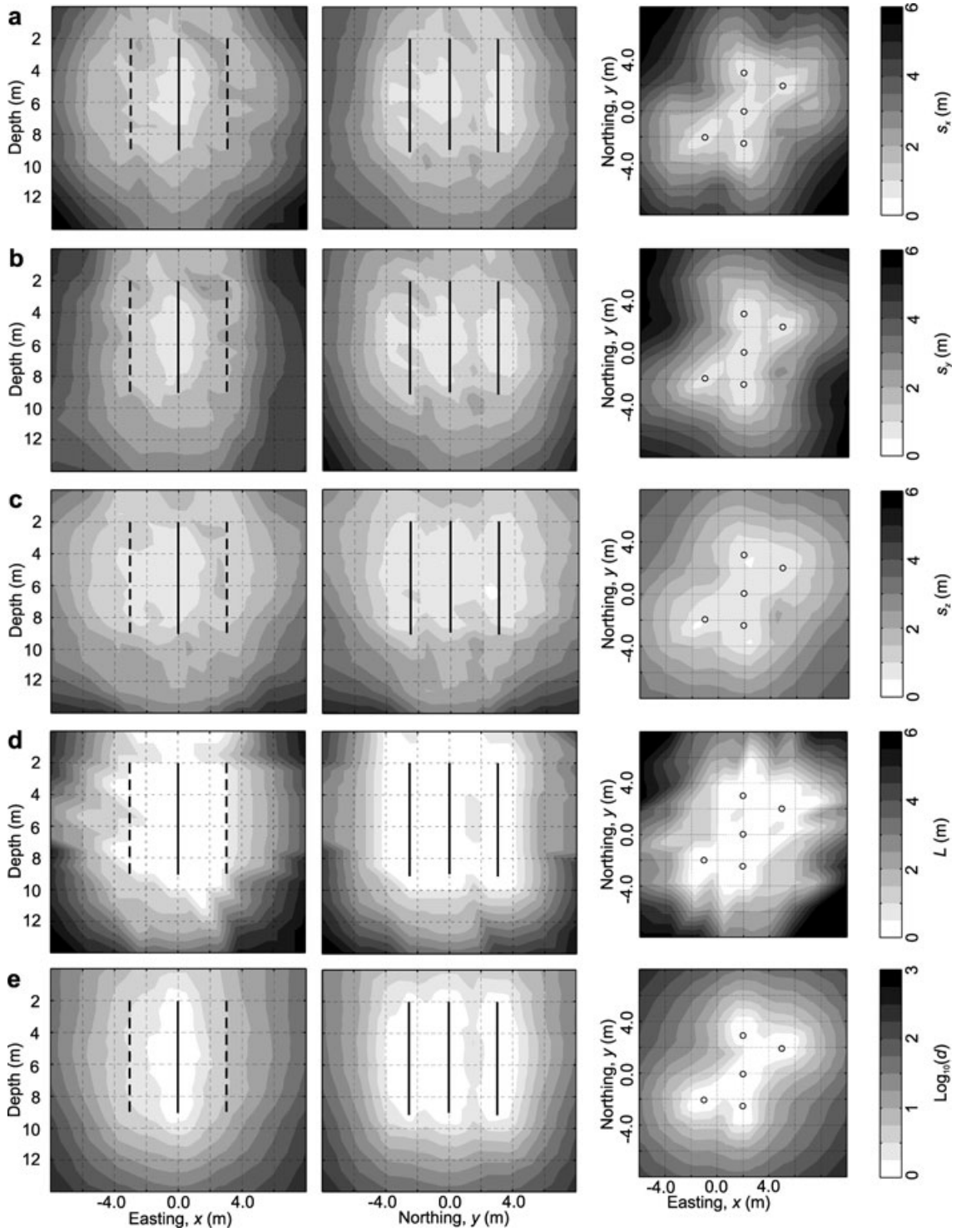

Figure 7. 3-D small-scale synthetic PSF attributes. (a)–(c) Directional spreads in x, y and z. (d) Localization error. (e) Departure from a delta function. Horizontal slices are taken at 5.5 m depth.

example, we have superior resolving capability in the northing section and in the vertical direction. Within the interborehole region, vertical spreads are less than 1 m. The horizontal s_x and s_y are approximately 1–2 m with $s_x > s_y$. Localization errors are typically confined to the horizontal plane with a magnitude less than the diagonal cell width of 0.35 m. These results suggest that we have the capability to resolve metre-scale preferential flow paths that are at least 1 m thick, with 1–2 m of horizontal extent, as observed in the recovered model (Fig. 8).

The PSFs illustrated in Fig. 9 are representative in character of those obtained over most of the vertical borehole extent. However, we do observe some variation in the PSF attributes with depth as illustrated in Fig. 11 for the directional spreads. This variability is understandable given the variability inherent to experimental data

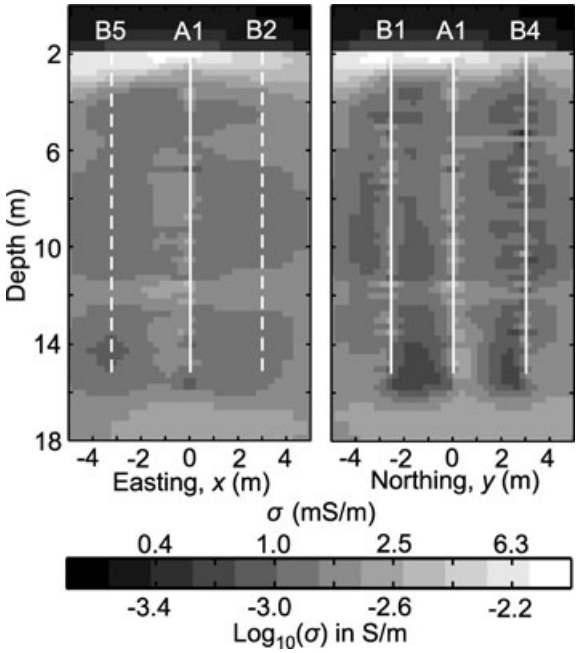

Figure 8. Cross-sections of estimated electrical conductivity for the background pre-injection experimental stage. Dashed vertical lines indicate out-of-plane boreholes; solid vertical lines indicate in-plane boreholes.

and the heterogeneity of the earth model (Fig. 8). In general, the observation of $s_x > s_y > s_z$ is consistent with depth, and below 16 m depth, the directional spreads increase significantly.

Although the spread can be used as relative resolution scale with meaningful units, interpretation of the spread as 'the' resolution can be hampered by off-diagonal features such as the asymmetry and oscillation of the PSFs apparent in Fig. 9 (and in other PSFs not shown). Any off-diagonal features of the PSF indicate that the actual model parameter m_k at $\mathbf{r}_k$ is being partitioned to other portions of the model domain according to eq. (9). Such complicated PSF behaviour is often not apparent from attribute analysis alone.

Some of the strongest off-diagonal features and oscillation of the PSFs seem to correlate with the borehole geometry. These borehole spikes and oscillations indicate partitioning of the off-borehole model parameter to near-borehole parameters. In effect, an artefact is being created, and PSF analysis allows for identification of potential artefact-contaminated regions such as the near-borehole region. We observe these vertically oriented borehole artefacts in the recovered pre-injection conductivity model (Fig. 8, northing) and in the synthetic models (the artefacts are not visible with the colour scale of Fig. 3). Because the synthetic model does not include fluid filled boreholes, the fact that we observe similar PSF spikes and vertical artefacts for the experimental and synthetic data suggests that the features are more precisely near-electrode artefacts, associated with the very high point sensitivity.

5.2 Post-injection PSFs

Recovered models for the post-injection data clearly image the elevated conductivity in the aquifer. For illustrative purposes, the solute plume itself is isolated via post-inversion parameter differencing (Fig. 12). The plume is clearly visible along the extent of the borehole and appears to have a greater width in the easting direction.

The 3-D post-injection PSFs are very similar to the synthetic PSFs (Fig. 4), but with more significant off-diagonal features (not

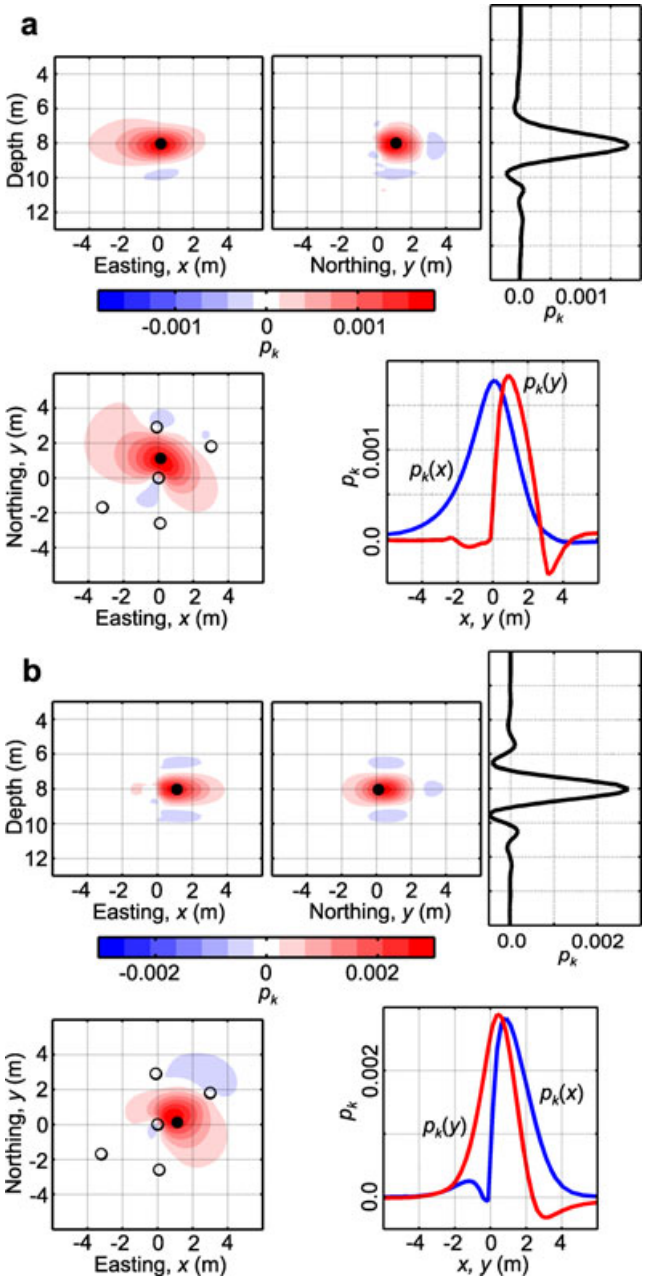

Figure 9. Pre-injection PSFs at positions indicated by the black dots: (a) $\mathbf{r}_k$ = [0.125, 1.125, 8.025], (b) $\mathbf{r}_k$ = [1.125, 0.125, 8.025]. The 2-D sections and 1-D profiles are taken through $\mathbf{r}_k$. Borehole locations are indicated by open circles.

shown). Similarly, the 1-D attributes are similar to the synthetic attributes, but with more variability. As illustrated in Fig. 13 for the post-injection attributes, we have the familiar pattern of borehole-controlled resolving capability. Also similar to the synthetic and pre-injection cases, the attributes for the easting section (not shown) exceed those for the northing section. Although we have no ground truth in the experimental case, the reduced easting resolution may be responsible for over-extent of the tracer boundary in the easting direction, so that the apparent asymmetry of the plume (Fig. 12) may not be entirely real.

Comparision of Fig. 13 with Fig. 10 illustrates the model dependence of the PSF between the post- and pre-injection stages. Although differences in the attributes are due explicitly to the change

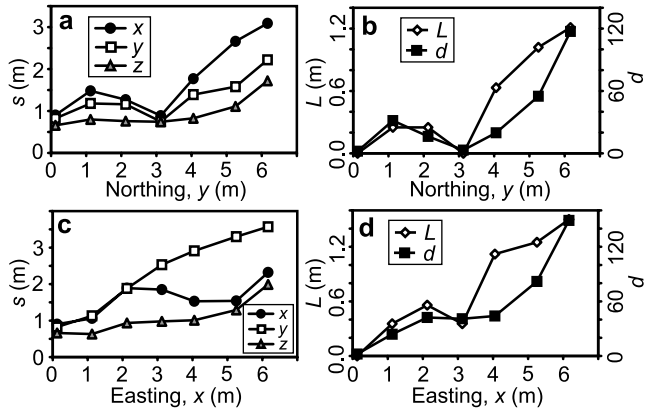

Figure 10. Pre-injection PSF attributes at 8.025 m depth. (a) Directional spreads in the northing direction. (b) Localization error and departure from a delta function in the northing direction. (c) Directional spreads in the easting direction. (d) Localization error and departure from a delta function in the easting direction.

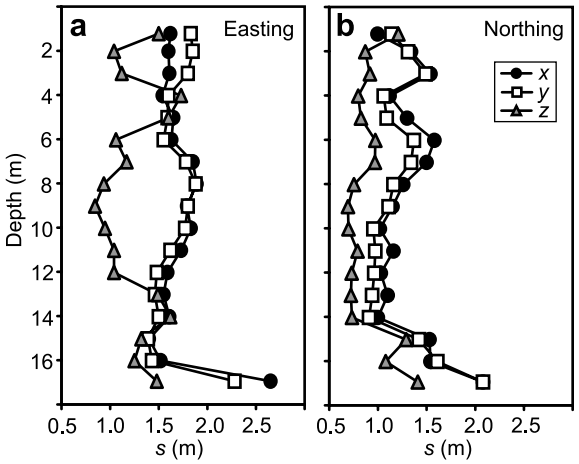

Figure 11. Pre-injection directional spreads in the vertical direction at (a) $x = 2.125$ m, $y = 0.125$ m (easting section) and (b) $x = 0.125$ m, $y = 2.125$ m (northing section).

in the model, we note that the data, the relative noise and the trade-off parameter have also changed, all of which contribute to $\mathbf{p}_k$. Systematic behaviour is hard to identify, but we make the following observations regarding the case-specific model dependence: (1) the post-injection spreads decrease, more so in the northing section; (2) the post-injection localization error increases in the interborehole region and (3) the post-injection departure increases in the interborehole region.

These observations are generally consistent in both the horizontal and vertical directions and have implications for the quantitative applicability of differential models such as Fig. 12. If the model dependence is significant, the resolution of the pre- and post-change models will be different and model differencing will be unstable (Oldenborger *et al.* 2007a). The resultant model change will have some bias that results from that change in resolution, as opposed to the change in model alone. In this fashion, model-dependent resolution may explain some of the inaccuracy of mass estimates obtained from post-inversion model differencing for ERT experiments (Oldenborger *et al.* 2007a), and model-dependent resolution should be a consideration for any differential geophysical experiment.

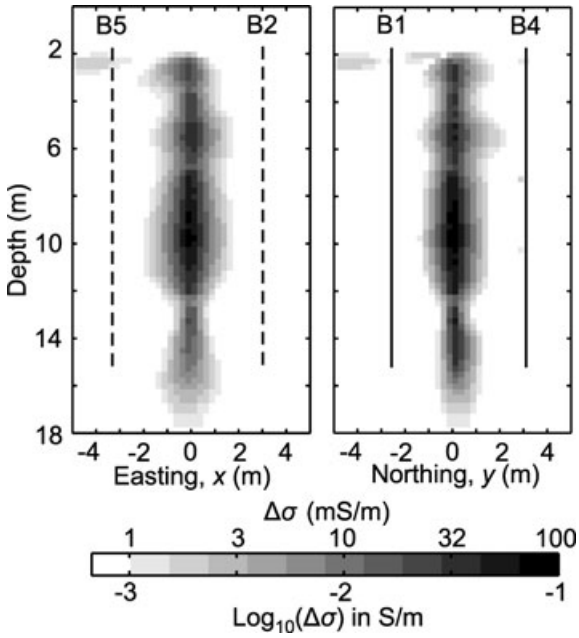

Figure 12. Cross-sections of estimated change between post- and pre-injection electrical conductivity. Dashed vertical lines indicate out-of-plane boreholes; solid vertical lines indicate in-plane boreholes.

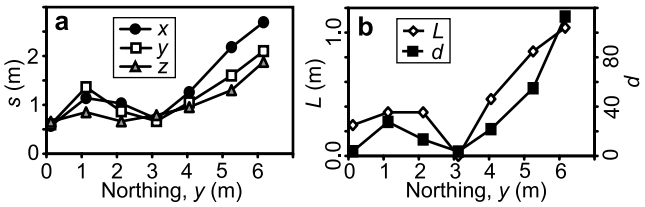

Figure 13. Post-injection PSF attributes in the northing direction at 8.025 m depth. (a) Directional spreads. (b) Localization error and departure from a delta function.

6 CONCLUDING DISCUSSION

The resolution component of solution appraisal involves investigating the relationship between our estimated model and the actual model. Determination of the full model resolution is difficult for multiscale 3-D problems due to both the large size of the matrices and matrix products involved and the amount of information generated. Alternatively, computation and analysis of the parameter-specific PSFs are useful for assessing the resolving capability and the reliability of model estimates obtained from 3-D ERT experiments.

The 3-D ERT problem is too large for computation of the entire set of PSFs, but we have shown how small subsets can provide useful information. In particular, examination of interborehole PSFs illustrates the Gaussian-like nature of the PSFs with significant directional asymmetry. The resolving capability of the ERT experiment is observed to be spatially variable and dependent on the electrode infrastructure, which is interpreted as a strong dependence on the geometric component of the sensitivity distribution for the 3-D DC resistivity experiment.

The 3-D PSFs are also characterized by off-diagonal features such as side-lobes and localization error. These off-diagonal effects would remain undetected with appraisal techniques based only on the diagonal of the resolution matrix. Similarly, analysis based solely

on attributes will indicate model parameters with low resolution but will not illuminate the potential mapping of those parameters to other portions of model space. It is through examination of the PSF in 3-D that we can identify the near-electrode regions as regions of high resolving capability, but also as recurring zones of off-diagonal PSF energy, which represent the formation of near-electrode (near-borehole) artefacts.

These observations underscore the fact that a single PSF does not describe the final estimated model—it is the impulse response for a single parameter among hundreds of thousands. Although a PSF does tell us how the Earth is locally resolved by the inverse procedure, when taken alone, it does not give us a precise indication of the final reconstructed model. For example, localization errors (primarily in the horizontal plane) are observed to approach the same order as the target dimensions in some cases. Nevertheless, synthetic examples routinely result in estimated conductivity models that are in good agreement with actual model, which suggests that no obvious misplacement of conductivity structure occurs to the extent, or with the pattern indicated by the localization errors. The implication is that localization errors are not so important that our actual models are not reasonably recovered; this sentiment is echoed by the demonstrated success of ERT applications.

In the fashion presented herein, the potential exists to routinely apply the PSF to 3-D ERT experiments as a method of solution appraisal. The PSF can be utilized to answer questions regarding feature discrimination and model reliability. The PSF can also be applied to aspects of the inverse problem such as survey design or to investigate the effects of data noise, regularization or model parametrization. We re-iterate that the PSF presented here is linearized. A such, results are model-specific and some features of the PSF may be a manifestation of the non-linearity of the problem.

ACKNOWLEDGMENTS

This research was funded by the Natural Sciences and Engineering Research Council of Canada, the Inland Northwest Research Alliance, EPA grant X970085-01-0 and NSF-EPSCOR grant EPS0132626. D. Oldenburg and the University of British Columbia Geophysical Inversion Facility provided DCIP3-D, a program library for forward modelling and inversion of DC resistivity and induced polarization data over 3-D structures, developed under the consortium research project: Inversion of 3-D Resistivity and Induced Polarization Data. We would like to thank A. Curtis and two anonymous reviewers for their constructive comments.

REFERENCES

Alumbaugh, D.L. & Newman, G.A., 2000. Image appraisal for 2-D and 3-D electromagnetic inversion, *Geophysics,* **65,** 1455–1467.

Backus, G. & Gilbert, F., 1968. The resolving power of gross Earth data, *Geophys. J. R. astr. Soc.,* **16,** 169–205.

Backus, G. & Gilbert, F., 1970. Uniqueness in the inversion of inaccurate gross Earth data, *Phil. Trans. R. Soc. Lond., A,* **266,** 123–192.

Barrash, W. & Clemo, T., 2002. Hierarchical geostatistics and multifacies systems: Boise Hydrogeophysical Research Site, Boise, Idaho, *Water Resour. Res.,* **38,** doi:10.1029/2001WR001259.

Dey, A. & Morrison, H.F., 1979. Resistivity modeling for arbitrarily shaped three-dimensional structures, *Geophysics,* **44,** 753–780.

Friedel, S., 2003. Resolution, stability and efficiency of resistivity tomography estimated from a generalized inverse approach, *Geophys. J. Int.,* **153,** 305–316.

Golub, G.H. & Van Loan, C.F., 1996. *Matrix Computations*, 3rd edn, John Hopkins University Press, Baltimore, MD.

Li, Y. & Oldenburg, D.W., 2000. 3-D inversion of induced polarization data, *Geophysics,* **65,** 1931–1945.

Menke, W., 1989. *Geophysical Data Analysis, Discrete Inverse Theory*, revised edn, Academic Press, San Diego, CA.

Miller, C.R. & Routh, P.S., 2007. Resolution analysis of geophysical images: comparison between point-spread function and region of data influence measures, *Geophys. Prospect.,* **55,** 835–852.

Nolet, G., Montelli, R. & Virieux, J., 1999. Explicit, approximate expressions for the resolution and a posteriori covariance of massive tomographic problems, *Geophys. J. Int.,* **138,** 36–44.

Oldenborger, G.A. & Routh, P.S., 2006. Theoretical development of the differential scattering decomposition for the 3D resistivity experiment, *Geophys. Prospect.,* **54,** 463–473.

Oldenborger, G.A., Routh, P.S. & Knoll, M.D., 2005. Sensitivity of electrical resistivity tomography data to electrode position errors, *Geophys. J. Int.,* **163,** 1–9.

Oldenborger, G.A., Knoll, M.D., Routh, P.S. & LaBrecque, D.J., 2007a. Time-lapse ERT monitoring of an injection/withdrawal experiment in a shallow unconfined aquifer, *Geophysics,* **72,** F177–F187.

Oldenborger, G.A., Routh, P.S. & Knoll, M.D., 2007b. Model reliability for 3D electrical resistivity tomography: application of the volume of investigation to a time-lapse monitoring experiment, *Geophysics,* **72,** F167–F175.

Oldenburg, D.W., 1983. Funnel functions in linear and nonlinear appraisal, *J. geophys. Res.,* **88,** 7387–7398.

Park, S.K. & Van, G.P., 1991. Inversion of pole-pole data for 3-D resistivity structure beneath arrays of electrodes, *Geophysics,* **56,** 951–960.

Parker, R.L., 1994. *Geophysical Inverse Theory*, Princeton University Press, Princeton, NJ.

Pascual-Marqui, R.D., 1999. Review of methods for solving the EEG inverse problem, *Int. J. Bioelectromag.,* **1,** 75–86.

Press, W.H, Teukolsky, A.A., Vetterling, W.T. & Flannery, B.P., 1992. *Numerical Recipes in Fortran 77, The Art of Scientific Computing*, 2nd edn, Cambridge University Press, New York, NY.

Ramirez, A., Daily, W., LaBrecque, D., Owen, E. & Chesnut, D., 1993. Monitoring and underground steam injection process using electrical resistance tomography, *Water Resour. Res.,* **29,** 73–87.

Ramirez, A.L., Daily, W.D. & Newmark, R.L., 1995. Electrical resistance tomography for steam injection monitoring and control, *J. Environ. Eng. Geophys.,* **0,** 39–52.

Routh, P.S., Oldenborger, G.A. & Oldenburg, D.W., 2005. Optimal survey design using the point spread function measure of resolution, *SEG (Expanded Abstracts),* **24,** 1033–1036.

Scales, J.A. & Snieder, R., 2000. The anatomy of inverse problems, *Geophysics,* **65,** 1708–1710.

Snieder, R., 1998. The role of nonlinearity in inverse problems, *Inv. Prob.,* **14,** 387–404.

van Wijk, K., Scales, J.A., Navidi, W. & Tenorio, L., 2002. Data and model uncertainty estimation for linear inversion, *Geophys. J. Int.,* **149,** 625–632.

Zhang, J., Mackie, R.L. & Madden, T.R., 1995. 3-D resistivity forward modeling and inversion using conjugate gradients, *Geophysics,* **60,** 1313–1325.

Zhou, B. & Greenhalgh, S.A., 2001. Finite element three-dimensional direct current resistivity modelling: accuracy and efficiency considerations, *Geophys. J. Int.,* **145,** 679–688.